# Opposite changes in Arctic and Antarctic sea-ice internal variability under anthropogenic global warming

Siou-Min Tsao[1], Yu-Chiao Liang[1], Clara Deser[2], and Jin-Yi Yu[3]

[1]Department of Atmospheric Sciences, National Taiwan University, Taipei, Taiwan

[2]National Center for Atmospheric Research Climate and Global Dynamics, Boulder, Colorado

[3]Department of Earth System Science, University of California-Irvine, Irvine, CA, USA

**Abstract (200 words)**

Sea-ice loss is a key indicator of anthropogenic climate change; however, internal variability may both obscure this mean-state signal and itself respond to human-induced global warming. Here we examine the changes in Arctic and Antarctic sea-ice internal variability over the period 1850-2050 using large-ensemble simulations. The magnitude of internal fluctuations in Arctic sea-ice area increases by $1.51 \times 10^{-3}$ million $km^2 \cdot year^{-1}$ in contrast to the Antarctic where it decreases by $1.13 \times 10^{-3}$ million $km^2 \cdot year^{-1}$ over 1970-2050 period. The opposite trends closely link to the level of sea-ice mean state, particularly when sea-ice extent is lowest, together with the peak values shifting toward later seasons. Snapshot empirical orthogonal function analysis reveals the spatiotemporal association of large-scale atmospheric and oceanic conditions accompanying the changes in sea-ice internal variability. As global warming intensifies, the weakening of tropical and North-Pacific sea-surface temperatures and the altered atmospheric circulation are accompanied with the increase of Arctic sea-ice internal

variability. In the Antarctic, an enhanced wave-train pattern from tropical Indian Ocean to Antarctic Peninsula relates to the decrease of its sea-ice internal variability. Our findings highlight the importance of changes in sea-ice internal variability under continued global warming, which carries significant implications for an accurate prediction of future sea-ice evolution.

Key words: sea-ice internal variability; large-ensemble climate model simulations; large-scale atmospheric and oceanic variabilities

# Introduction

Recent loss of sea ice in the polar regions is among the most striking consequences of anthropogenic global warming[1]. Within the northern and southern polar circles, the loss of Arctic and Antarctic sea ice is consequential for nearby terrestrial and marine ecosystems[2-6], coastal protection[7,8] and socio-economic impacts[9-11]. The sea-ice declines in the two polar regions may also have far-reaching effects on the large-scale atmospheric circulation[12-16], climate variability[17-25], and the global energy budget[13,26-30].

Since routine satellite observations began in 1978, Arctic sea-ice area (SIA) and volume have declined in all seasons[31]. While the largest Arctic SIA loss has occurred in September at a rate of 0.45 million $km^2 \cdot year^{-1}$ during the 1979-2024 period[32], the sea-ice declining rate has been slowdown in the past two decades[33]. The evolution of Arctic SIA decline, thus, underwent a complex trajectory rather than monotonical decrease. Antarctic SIA has also undergone a complex temporal evolution. Annual-mean Antarctic SIA increased slightly (0.02 million $km^2 \cdot year^{-1}$) during 1979-2015, opposing the secular global warming[34, 35]. However, since 2016, Antarctic SIA has declined precipitously, with a loss rate of 0.12 million $km^2 \cdot year^{-1}$ (during 2015-2023), and reached a record minimum in 2023[35]. This abrupt transition after 2015 has prompted speculation that Antarctic sea ice is entering a new climate regime[36-38].

The stark interhemispheric contrast in Arctic and Antarctic sea-ice evolutions has prompted growing interests in the causes and underlying mechanisms. Previous studies have revealed the important role of internal variability – emerging from the coupling between the atmosphere, ocean, cryosphere, land components in the Earth system[39] - in modulating sea-ice change[40,41]. For example, in the Arctic, by comparing large-ensemble climate model simulations with observations indicated that the recent observed

slowdown in September Arctic sea-ice decline is consistent with internal variability[33]. In the Antarctic, studies have attributed the abrupt decline of sea-ice extent to shifts in low-frequency modes of climate internal variability such as Pacific Decadal Variability (PDV) and Atlantic Multi-decadal Variability (AMV)[34,42]. Indeed, such intrinsic variability can mute or amplify the forced response to global warming[43-47], adding considerable uncertainty to future projections[48,49]. The unpredictable nature of internal variability further complicates the accurate seasonal sea-ice prediction[50], robust assessment of sea-ice evolution[33,51-53] and hinders the development of effective climate adaptation and risk mitigation strategies for sea-ice loss[54,55]. While efforts have been paid on characterizing and quantifying the mean state sea-ice response to anthropogenic forcing, the understanding of the changes in sea-ice internal variability, its spatial pattern, seasonal evolution, and associated large-scale circulation changes under a warming climate can be revisited and advanced using new generation of climate models.

The Community Earth System Model version 2 (CESM2) Large Ensemble (CESM2-LE) under historical and future (SSP3-7.0) radiative forcing[56] provides a valuable simulation set with large-ensemble members to assess the changes in SIA internal variability during the historical and future periods (see Methods). Each of the 50 members of the CESM2-LE is subject to the same radiative forcing, but begins from a different initial condition, leading to ensemble spread to represent internal variability[43,57-59]. To isolate forced changes in internal variability from forced changes in the mean state, we subtract the ensemble-mean from each member and then calculate the standard deviation ($\sigma$) of the residuals across the members at each time step. In this way, we leverage the large number of samples (50) of internal variability that exists at any given time in the CESM2-LE to identify any evolving forced changes in the amplitude of internal variability (given by $\sigma$

(t)) from 1850-2050. We start by highlighting the contrasting seasonal evolution of SIA σ (t) between the Arctic and Antarctic, and relating these to the mean-state changes in CESM2-LE. We also apply the same analysis to other large-ensemble simulation sets conducted by different climate models to investigate the robustness of the results simulated by CESM2. We finally examine the global atmospheric and oceanic conditions associated with forced changes in SIA internal variability to gain further insight and understanding.

# Results

## The evolution of Arctic and Antarctic sea-ice internal variability under external forcing

We begin by examining the internal variability of annual sea-ice area (SIA; see Methods) for the two polar regions as simulated by the CESM2-LE over the 1850–2050 period (blue lines in Figs. 1a and 1b). The Arctic and Antarctic show striking differences in their evolution of SIA internal variability (SIA σ(t): blue lines in Figs. 1a and 1b), estimated as the standard deviation across 50 ensemble members for each year (i.e., grey shading in Figs. 1a and 1b). Prior to the 1970s, Arctic and Antarctic SIA internal variability fluctuated around 0.3 million km$^2$ with small long-term (1850-1969) trends of $-3.56 \pm 1.86 \times 10^{-4}$ and $-1.39 \pm 1.78 \times 10^{-4}$ million km$^2$·year$^{-1}$, respectively. However, thereafter, Arctic SIA σ(t) increases steadily while Antarctic SIA σ(t) decreases gradually. Consequently, there is an increasing long-term trend in Arctic SIA σ(t) of $1.56 \pm 0.38 \times 10^{-3}$ million km$^2$·year$^{-1}$, and a decreasing trend in Antarctic SIA σ (t) of $1.13 \pm 0.33 \times 10^{-3}$ million km$^2$·year$^{-1}$ over the period 1970-2050. These contrasting trajectories of sea-ice internal

variability are somewhat counterintuitive under ongoing global warming, in particular when their ensemble-means show accelerated decreasing trends after 1970 (grey lines in Figs. 1a and 1b, 1850-1969 trends for Arctic and Antarctic SIA are $2.84 \pm 0.67 \times 10^{-3}$ and $-4.47 \pm 0.43 \times 10^{-3}$ million km$^2$·year$^{-1}$ they; whereas their trends become $4.05 \pm 0.14 \times 10^{-2}$ and $-3.55 \pm 0.07 \times 10^{-2}$ million km$^2$·year$^{-1}$ during 1970-2050), reflecting the forced response to anthropogenic and natural radiative forcings. The above analysis indicates that early 1970s is the key timing to separate the trajectory of Arctic and Antarctic SIA internal variability and mean state and the 1970-2050 period will be the focus of the following analysis. A fundamental question then arises: why does SIA internal variability evolve so differently in the Arctic and Antarctic despite similar modeled mean state SIA declines after 1970s?

To answer this question, we examine the monthly evolution of SIA internal variability (color shadings in Figs. 1c and 1d). Sea-ice internal variability in both polar regions exhibits distinctive seasonal characteristics. Over the 19$^{th}$ and 20$^{th}$ centuries, internal variability in the Arctic peaks during August-October when the climatological mean SIA is at its seasonal minimum, and is lowest during February-April when mean SIA is at its seasonal maximum. After 2020, peak Arctic SIA $\sigma(t)$ intensifies and shifts to earlier (July) and later (October-November) months, following the evolution of mean SIA (black contour lines), and resulting in the largest trends in variability during July and October-December (right panel). However, as the mean Arctic SIA in August and September declines to near ice-free conditions by around 2030 (defined here as SIA<1 million km$^2$, indicated by magenta contour lines), internal variability sharply decreases, leading to a near-zero and negative long-term trends respectively. In contrast, Antarctic SIA $\sigma(t)$ peaks during March-May when mean SIA is growing rapidly from its seasonal minimum

in February. Like the Arctic, peak SIA σ(t) in the Antarctic exhibits a migration toward earlier and later months over time after the 1970s. However, unlike the Arctic, the Antarctic experiences a general weakening of internal variability across all months, with the most pronounced decreases occurring in February and March, coinciding with near ice-free conditions after around 2030. These contrasting trends suggest that Arctic and Antarctic sea-ice variability respond differently to ongoing global warming, likely reflecting distinct underlying processes and interactions with regional and global climate systems.

The seasonal coherence between the evolution of internal variability and mean-state SIA suggests that internal variability may be fundamentally linked to the concurrent sea-ice mean state, as previous studies revealed[41,49]. To investigate this relationship, we examine the strength of internal variability as a function of the mean SIA during the months of minimum SIA in each hemisphere (Fig. 2). In the Arctic, internal variability initially increases as SIA declines, plateaus when SIA ranges between approximately 2.5 and 4.5 million $km^2$, and subsequently decreases as SIA continues to recede across August, September, and October (Figs. 2a–c). This behavior yields a parabolic relationship between SIA internal variability and SIA. Spatial patterns of internal variability offer further insights into this nonlinearity: regions of maximum internal variability (blue shading in Fig. 3) consistently align with the mean sea-ice edge (red contours in Fig. 3), highlighting that internal variability is maximized in the zones with partial ice cover, rather than areas of near-total absence (i.e., 0% SIC) or full coverage (i.e., 100% SIC). Indeed, the number of ocean grid cells with intermediate SIC (10–90%) peaks when total SIA falls within the 2.5–4.5 million $km^2$ range and declines when SIA becomes either too low or too high. Geographical constraints likely modulate this relationship; in the Arctic,

the southern land boundary encircling the ocean limits sea-ice expansion under colder conditions, thereby suppressing variability.

In contrast, the Antarctic displays a strikingly linear relationship across all selected months (Figs. 2d–f), with internal variability scaling proportionally to mean SIA. Unlike the Arctic, Antarctic sea ice can expand northward without terrestrial barriers (Fig. 3), allowing internal variability to increase continuously under colder climates. The number of ocean grid cells with intermediate SIC (10–90%) in the Southern Ocean gradually decreases as the mean SIA declines with time. This hemispheric contrast underscores the role of geographic ice-edge configurations in shaping the evolution of sea-ice internal variability under climate change, consistent with previous studies using simpler or previous generation of climate models[41,60].

While the findings presented above are based on simulations by CESM2, we recognize that sea-ice biases in CESM2 have been reported, including thinner sea-ice thickness and resultant less sea-ice extent with respect to observations[61,62]. Therefore, it is crucial to assess their robustness across different climate models and evaluate potential model dependencies. To this end, we examine the long-term trends of sea-ice internal variability simulated by eight additional CMIP5/6 models over the 1850–2050 period (see Methods and Supplementary Fig. 1). Overall, these models broadly reproduce the contrasting trends observed in CESM2-LE, with increasing Arctic sea-ice internal variability and decreasing Antarctic variability. However, models suffering from substantial biases in mean SIA show weaker or inconsistent trends. For example, CSIRO-Mk3.6, characterized by unrealistically extensive Arctic SIA and muted sea-ice decline over the analysis period (Supplementary Fig. 1), shows minimal trends in Arctic SIA internal variability. We also include the high-resolution version of CESM1-LE simulation[63], which also shows similar

results to the CESM2-LE for the Arctic SIA internal variability trend, but opposite for the Antarctic one. Looking into its seasonal evolution indicates that the months with large SIA internal variability are during June-November and the trends during these months are opposite from models with lower resolutions (Supplementary Fig. 2). This is interesting as the spatial resolution seems more critical for the Antarctic sea-ice internal variability than the Arctic counterpart. Further analyses are needed to investigate the cause.

To further disentangle the contributions from different climate forcings, we analyze CESM2 single-forcing large ensembles (see Methods and Supplementary Fig. 3). Results reveal that GHG forcing is the dominant driver of the decreasing Antarctic SIA trends, while the Arctic has minimal sea ice due to strong warming effect and the resultant trend is negative. The anthropogenic aerosols induce small negative trends in Arctic SIA internal variability, likely reflecting the aerosol reduction in the North American and Europe after 1970s. Interestingly, forcings other than the above combined (volcanic forcings, solar irradiance, ozone, land-use change, etc.) contribute to increasing sea-ice variability trends in both polar regions, a result that, while beyond the immediate scope of this study, warrants further investigation.

To elucidate the processes underlying the seasonal evolution of sea-ice internal variability in the Arctic and Antarctic, we analyze the contributions of radiative and turbulent surface heat fluxes. Notably, interannual variability in shortwave radiation exhibits similar long-term trends to that of SIA in both polar regions (not shown), suggesting a potential causal relationship. Seasonally, the Arctic displays enhanced shortwave variability from April to September, while the Antarctic shows reductions from January to March (Supplementary Figs. 4a and b). These timing patterns largely mirror seasonal changes in albedo internal variability (Supplementary Fig. 5) and

precede the corresponding SIA internal variability by one to two months, implicating the sea-ice albedo feedback as a driver of enhanced or reduced sea-ice internal variability. By contrast, variability in longwave radiation and latent heat fluxes lags behind SIA variability, suggesting these are likely responses to, rather than drivers of, sea-ice internal variability changes (Supplementary Figs. 6 and 7). Interestingly, sensible heat fluxes appear to partially offset the latent heat flux contributions (Supplementary Fig. 8). This compensation may arise from a reduced thermal contrast between the ocean surface and the atmosphere under amplified Arctic warming during the cold season. Another important factor is sea-ice thickness. The sea-ice-thickness internal variability in both polar regions exhibits negative trends in most months except summer (Supplementary Fig. 9), suggesting that its variability may be stabilized by the negative feedback of conductive heat fluxes[64,65] and may also be influenced by strong albedo variability when sea ice becomes thinner and less extensive during summer.

Taken together, these additional analyses suggest that a chain of processes during spring and summer associated with reductions in mean sea-ice coverage amplify shortwave absorption, enhancing internal variability during the melt season. This enhanced variability then persists into the cold season via delayed longwave radiative and latent heat fluxes, thereby sustaining the enhanced sea-ice variability. In addition, increased variability in sea-ice thickness may develop later, when thinner sea ice allows larger internal variability to develop.

**The large-scale atmospheric and oceanic variability associated with the changes in sea-ice internal variability**

In addition to local thermodynamic and dynamic processes, sea-ice variability can be also influenced by large-scale atmospheric and oceanic variability modes[14,27,42,66-73]. Conversely, growing evidence suggests that sea-ice variability itself can exert remote impacts on midlatitude and tropical climate via both atmospheric teleconnections and oceanic pathways[12-20]. To investigate these bidirectional interactions, we apply a snapshot empirical orthogonal function (SEOF) analysis (see Methods) to the internal component of SIC anomalies in the Arctic and Antarctic. This approach captures the leading spatial patterns of internal sea-ice variability across the ensemble members at each time step, and, critically, enables a statistically coherent assessment of their co-variability with large-scale atmospheric and oceanic anomalies outside the polar regions. We focus on the leading mode (Supplementary Fig. 10) of SIC anomalies during the sea ice minimum season - August to October for the Arctic and January to March for the Antarctic - when the change in internal variability is most pronounced. To ensure temporal robustness, SEOF is applied within a moving 5-year window across the ensembles following O'Brien and Deser (2023)[74] We then regress sea-level pressure (SLP) and sea-surface temperature (SST) anomalies onto the principal component of the leading SEOF mode (hereafter SPC) during three distinct time periods to examine how large-scale circulation and ocean patterns co-evolve with sea-ice internal variability under external forcings.

In the early historical period of the 1850s, the leading SEOF mode of SIA reveals a dipole structure in the Arctic, with negative anomalies concentrated in the East Siberian and Laptev Seas and positive anomalies spanning the northern Barents Sea, Svalbardian archipelago, and eastern Greenland (Fig. 4a). These anomalies are tightly aligned with the mean sea-ice edge (green contour line in Fig. 4a), highlighting the correspondence of

marginal ice zones and sea-ice internal variability. The regression pattern of SLP anomalies shows a localized reduction over the East Siberian–Chukchi Seas (Fig. 4d), consistent with a thermally forced heat-low response to regional sea-ice loss[66,75,76]. Beyond the Arctic, a coherent SLP anomaly appears over the North Pacific, coupled with an arc-shaped SST pattern that resembles, respectively, known features of the North Pacific Oscillation (NPO)[77] and North Pacific Gyre Oscillation (NPGO)[78] (Fig. 4g). Additionally, a weak El Niño–like SST anomaly emerges in the tropical Pacific, suggesting an Arctic-tropical Pacific teleconnection[79-81].

By the early 21st century, as the climate warms, the negative SIA anomalies shift poleward and become more centralized in the Arctic Ocean, while positive anomalies contract toward the eastern coast of Greenland (Fig. 4b). The corresponding regressed SLP and SST anomaly patterns intensify (Figs. 4e and 4h), indicating a strengthening of the sea-ice coupling with extratropical and tropical ocean–atmosphere variability under anthropogenic warming. However, by the 2040s, this connection begins to break down. The center of SIA anomalies migrates further toward the central Arctic and weakens (Fig. 4c), while the El Niño–like SST signal in the tropical Pacific nearly disappears and the NPGO-like signal in the North Pacific weakens (Fig. 4i). Together, these results suggest that Arctic sea-ice internal variability is linked to both North Pacific and tropical Pacific variability, but that the strength of this linkage depends on the spatial distribution and amplitude of sea-ice anomalies. When variability is concentrated along the Siberian marginal ice zone, the Arctic–Pacific connection strengthens; as sea-ice variability contracts toward the central Arctic, this Arctic-Pacific teleconnection is diminished.

In the Antarctic, the leading SEOF mode of sea-ice internal variability during the mid-19th century reveals widespread positive SIC anomalies encircling the continent, except for a

pronounced negative anomaly in the Bellingshausen Sea (Fig. 5a). The regressed SLP anomalies show elevated pressure over the Antarctic interior (Fig. 5d), consistent with enhanced easterly wind anomalies that promote near-coastal sea-ice accumulation via Ekman transport. Notably, a southeastward-propagating atmospheric wave train originating from the Maritime Continent and eastern Indian Ocean intersects with a wavenumber-3 pattern encircling the Southern Ocean. These features likely converge to produce positive SLP anomalies over the Amundsen and Bellingshausen Seas, and potentially contribute to the SIC dipole anomalies.

By the early 21st century, the influence of tropical variability strengthens: a robust El Niño–like SST signature emerges in the tropical Pacific, accompanied by enhanced SST anomalies in the Indian Ocean and tropical Atlantic (Figs. 5e and 5h). These atmospheric and oceanic changes signal intensified inter-basin teleconnections and a strengthening of the atmospheric teleconnection bridge linking the tropics to the Southern Ocean. As global warming progresses into the 2040s, these teleconnections become more pronounced. The El Niño–like SST pattern dominates the tropical Pacific and reinforces inter-basin coupling, which reorganizes the atmospheric circulation. The center of positive SLP anomalies shifts eastward toward the Antarctic Peninsula (Fig. 5f), altering the regional wind patterns and enhancing sea-ice loss to the east of the peninsula (Fig. 5c). This atmospheric reconfiguration also affects the extratropical patterns in the Northern Hemisphere, with a Pacific North America–like response over the North Pacific and a negative North Atlantic Oscillation–like signal over the North Atlantic sector, implying a stronger inter-basin interaction. We also analyze the 500-hPa geopotential height regressions and obtain consistent large-scale circulation patterns (Supplementary Fig. 11).

Taken together, the results underscore a decaying connection between tropical Pacific variability and Arctic sea-ice internal variability and increasing one between tropical Indian and Pacific Ocean variability and Antarctic sea-ice internal variability under a warming climate. They further suggest that, in addition to local atmospheric–oceanic feedbacks, evolving large-scale teleconnections could play a non-negligible role in shaping polar sea-ice internal variability.

## Discussion

Our findings highlight the importance of evolving changes in the characteristics of internal sea-ice variability under historical and future radiative forcing, with the most pronounced signals emerging during the months of minimum SIA in both hemispheres. As sea-ice area or extent in the warm season has been widely recognized as a critical factor in determining the annual sea-ice state[11,82,83], influencing local oceanic heat and carbon uptake[11], and modulating the occurrence of marine heatwaves[22], understanding its evolution and the mechanisms underlying changes in sea-ice internal variability is essential for robust and accurate projections of sea-ice evolution and its subsequent climate impacts at seasonal or longer timescales. Interestingly, sea-ice internal variability in the Arctic and Antarctic exhibit opposite long-term trends, raising the question: what gives rise to this asymmetry of internal variability under global warming?

Exploiting the 50-member CESM2 Large Ensemble over the period 1850-2050, which provides robust sampling of internal variability and an accurate estimate of the mean state at any given time, we demonstrate that The Arctic SIA internal variability shows a quadratic relation with its mean value, while a linear relationship emerges in the

Antarctic. This is due to the seasonal shifting of marginal ice zone in shaping internal variability in both polar regions. This provides a physically consistent explanation for the contrasting trends, arising from differences in geographical constraints between the Arctic and Antarctic. Indeed, while previous study proposed interhemispheric differences in the model projections can be attributed to differences in coastline geometry[60,84] other studies also emphasized the importance of the marginal ice zone fraction[85]. Additionally, integrating the perspectives with our findings - that overestimated or underestimated SIA in models relates to the degree of its internal variability - provides new insights into the model biases and future model development in simulating polar sea-ice mean state and variability[86].

From an energy-budget perspective, the internal variability of shortwave radiation (Supplementary Fig. 4), together with that of albedo (Supplementary Fig. 5), closely follows the variability of sea ice, consistent with previous studies showing a strong correspondence between absorbed shortwave radiation, ice melt, and the position of the ice edge[87]. As the distribution of sea ice can affect the Earth's energy budget[30], the shifting of the sea-ice spatial pattern associated with internal variability changes may have wider implications for global energy budget variations. Other than the radiative component, the contributions of the convergence of heat transported by ocean currents and atmospheric circulation[87,88] are not examined here and warrants further investigation. Interestingly, oceanic heat transport also exhibits an asymmetrical relationship with sea ice between the Arctic and Antarctic[89], revealing its relevance to the contrasting sea-ice internal variability changes in the two polar regions.

In this study, we also examine the large-scale atmospheric and oceanic patterns associated with the changes in sea-ice internal variability using SEOF analysis. We find

that the NPO-like pattern in the atmosphere and NPGO-like pattern in the ocean are associated with Arctic sea-ice internal variability, which may influence or be influenced by the tropical Pacific via atmospheric pathways[20,90-92]. However, this Arctic-tropical teleconnection greatly weakens after 2040s when global warming becomes stronger, as the center of action of sea-ice internal variability moves toward the central Arctic Ocean. In contrast, the association between Antarctic sea-ice internal variability and tropical ocean variability grows stronger as global warming continues. It seems to involve a wide range of tropical variability modes, including the Indian Ocean Dipole (IOD), Pacific sub-decadal SST variability, the Interdecadal Pacific Oscillation (IPO), ENSO, the Atlantic Niño, and combinations or inter-basin interactions thereof[93-97]. Indeed, when applying SEOF analysis to tropical Pacific SST to examine whether the leading SPCs (Supplementary Figs. 12 and 13) co-vary with the SPCs of polar sea ice, we find that the correlation between tropical Pacific SST and Antarctic sea-ice internal variability exhibits a positive trend under ongoing global warming, whereas no such trend is evident in the Arctic (Supplementary Fig. 14). This is consistent with previous studies showing that extra-polar influences on Antarctic sea ice often involve substantial oceanic contributions[15,70]. Recent coupled model experiments further suggest that, as anthropogenic forcing intensifies, the influence of deep convection weakens, while the Southern Annular Mode (SAM) plays an increasingly prominent role in Antarctic sea-ice variability[70]. Although the causality and linking mechanisms across timescales need further clarification and examination, our results suggest that the internally-driven Antarctic-tropical teleconnection intensifies in the upcoming decades, whereas the Arctic-tropical connection recedes.

Lastly, using satellite-derived SIA to calculate a 5-year running standard deviation as an estimate of sea-ice internal variability in observations (Supplementary Fig. 15), we find a significant increasing trend only in the Antarctic, which differs from the results based on the CESM2-LE (Fig. 1a, b). This discrepancy may arise because the observed record reflects a combination of externally forced changes and internal variability, requiring additional methods to separate these components. Interestingly, when performing the 5-year running standard deviation analysis for each member of CESM2-LE, the range of simulated Arctic SIA internal variability trends encompasses the observed trend (Supplementary Fig. 15c), indicating the observation trend may not occur by chance. In contrast, none of the ensemble members of CESM2-LE can capture the observed Antarctic SIA internal variability trend (Supplementary Fig. 15d), reflecting the remarkably unusual sea-ice decline in Antarctic after 2016[37,38]. When compared with satellite-based studies employing low-frequency component analysis over the observational period[68,69], our results for the early 21$^{st}$ century are consistent both in terms of variability magnitude and the spatial distribution of dominant variability. In the Arctic, regions exhibiting the strongest internally-driven variability in observations from 1979 to 2021 - particularly the East Siberian and Laptev seas - coincide with the locations of maximum anomalies along the retreating ice edge identified in CESM2 simulations (Fig. 4). Similarly, observational studies indicate that the western Antarctic sector exhibits large internal variability over the 1979–2022 period[69], a feature that is also evident in our SEOF results based on CESM2 (Fig. 5). Further analysis is needed to understand the origins of the observation-model consistency or discrepancy, including whether it may arise by chance due to the limited sampling of internal variability in the short observational record.

# Methods.

## CESM2 historical, future projection, and single-forcing large ensembles

We analyze simulations from the Community Earth System Model version 2 Large Ensemble (CESM2-LE)[56], conducted by the National Center for Atmospheric Research (NCAR). This suite of simulations includes a 1400-year pre-industrial control run, historical runs driven by CMIP6 forcing from 1850 to 2014, and projection runs under the Shared Socioeconomic Pathway (SSP) 3-7.0 forcing scenario after 2015. The spatial resolution is at a nominal 1°. We analyze 50 ensemble members with smoothed biomass burning (SMBB) emissions to avoid discontinuities in the biomass burning records, which have been shown to cause rapid sea-ice decline[98,99]. Monthly output fields of sea-ice concentration (SIC), sea-level pressure (SLP), and sea-surface temperature (SST) from 1850 to 2050 are used to separate internal variability from the forced response. The sea-ice area (SIA) is calculated by multiplying SIC over the ocean grid with the corresponding grid-cell area and summing over the Arctic (40°N-90°N) and Antarctic (50°S-90°S) domains respectively. A threshold of 15% SIC is applied to define the sea-ice edge[65,92].

We additionally use simulations from the CESM2 Single-Forcing Large Ensemble project from NCAR, which employs the same model configuration and forcings as the CESM2 Large Ensemble but isolates the roles of individual external forcings in historical and future changes[98]. These ensemble members were initialized in 1850 with the same initial conditions as CESM2-LE. In each experiment, only one forcing evolves in time, following CMIP6 historical forcing prior to 2015 and SSP3-7.0 trajectory thereafter, while all other forcings are fixed at 1850 values. The single-forcing experiments include well-mixed greenhouse gases (GHGs) with 15 members, anthropogenic aerosols (AAER) with 20

members, biomass burning aerosols (BMB) with 15 members, and "everything else," (EE, i.e., all other forcings including volcanic eruptions, solar irradiance changes, and land-use changes) with 15 members.

**CESM1 large ensembles and CESM1.3 high-resolution simulations**

To test the robustness, we also analyze simulations from the Community Earth System Model version 1 Large Ensemble (CESM1-LE) conducted at NCAR[100]. This dataset consists of a 40-member ensemble of full- coupled CESM1 simulations spanning 1920–2100 with a nominal 1° spatial resolution. The simulations use historical radiative forcing up to 2005, followed by the Representative Concentration Pathway (RCP) 8.5 scenario thereafter. We also analyze simulations from the high-resolution configuration of CESM version 1.3 (CESM1.3-HR), developed through the International Laboratory for High-Resolution Earth System Prediction (iHESP), a collaboration among the Qingdao National Laboratory for Marine Science and Technology (QNLM), Texas A&M University (TAMU), and NCAR[63]. The CESM1.3-HR ensemble includes 10 members, initialized from a 500-year pre-industrial control run and integrated under 1850–2005 historical forcing followed by the 2006–2100 RCP8.5 scenario. The simulations employ a nominal horizontal resolution of 0.25° for the atmosphere and land components, together with a 0.1° resolution for the ocean and sea-ice components. This dataset has been used in studying the amplified Arctic warming[101] and projecting the last ice area[102].

**Single-model initial-condition large ensembles (SMILEs)**

We use four models from the suite of seven single-model initial-condition large ensembles (SMILEs) in consideration of the size of the ensemble to generate the ensemble spread that estimate the effect of internal variability: CSIRO-Mk3-6-0 (30 members)[103], GFDL-CM3 (20 members)[104], GFDL-ESM2M (30 members)[105], and MPI-ESM (100 members)[106]. All the SMILE simulations are forced with CMIP5 historical forcing up to 2005 and the RCP8.5 scenario from 2006 to 2100. SMILEs have been utilized to study the seasonality and uncertainty of the Arctic amplification under GHG and aerosol forcings[107] and been shown to have good agreement with observations in terms of interannual sea-ice variability[108].

**Detection and Attribution Model Intercomparison Project (DAMIP)**

The Detection and Attribution Model Intercomparison Project (DAMIP)[109] is one of the project under CMIP6[110]. We use two datasets contained in the DAMIP repository as they provide large-ensemble members: The sixth version of the Model for Interdisciplinary Research on Climate (MIROC6; 50 members) was cooperatively developed by a Japanese modeling community[111] and the Canadian Earth System Model version 5 (CanESM5; 25 members) is developed at the Canadian Centre for Climate Modelling and Analysis (CCCma) at Environment and Climate Change Canada (ECCC)[112]. Both of them are simulated with the CMIP6 historical forcing before 2014 and the SSP 2-4.5 scenario thereafter till 2100. DAMIP has been used to quantify and project the effect of single forcings including GHGs and anthropogenic aerosols on Arctic temperature[113] and Arctic sea-ice loss[114].

## Observational data

For additional comparison analysis, we use sea-ice observations from the National Snow and Ice Data Center (NSIDC) Sea Ice Index Version 4[35] for the period of 1979–2025. The gridded sea-ice concentration fields are derived from passive microwave imagery.

## Snapshot empirical orthogonal function analysis

To investigate the spatial structure of internal variability and its evolution under global warming, we apply the snapshot empirical orthogonal function (SEOF) analysis to the ensemble simulations. Unlike traditional EOF analysis, which requires a subjective choice of a temporal window and may be sensitive to data non-stationarity[115], SEOF analysis is performed across the ensemble dimension at each individual time step. Specifically, the original data are structured as a four-dimensional array consisting of ensemble members, time, latitude, and longitude. At each time step, the instantaneous ensemble mean (i.e., the externally forced response) is removed and leaves only the internal variability component of the field, which characterizes the set of potential climate states permitted by the climate system at the given time instant[74]. To account for the convergence of meridians and the varying grid areas near the poles, the data are weighted by the square root of the cosine of latitude, following standard EOF analysis.

For robustness and less influence of short-term fluctuations in individual ensemble members, we apply a 5-year running time window in the SEOF analysis similar to a previous study[74]. This approach increases the sample size at each time step from 50 to 250 (i.e., 5 years × 50 ensemble members), the resulting spatial patterns are assigned to the central year of each window. Consequently, although the original data span from

1850 to 2050, the 5-year window SEOF results cover the period from 1852 to 2048. We also verify the possibility of mode mixture and confirm that higher-order modes are well separated from leading modes based on the North test[116].

The SEOF analysis is applied to SIC anomalies in the Arctic and Antarctic. For this purpose, we define the analysis domains as 40°N–90°N for the Arctic and 50°S–90°S for the Antarctic, covering the full latitudinal range of sea ice presence. Similar to traditional space-time EOF analysis, which produces mutually orthogonal spatial patterns and associated temporal principal components (PCs), space-ensemble SEOF analysis yields mutually orthogonal snapshot EOF patterns (SEOFs) and their corresponding snapshot PCs (SPCs) across the ensemble dimension. The SEOFs represent the dominant spatial structures of internal variability at a given time period, while the SPCs quantify their amplitude and sign across ensemble members. To explore large-scale factors associated with sea-ice variability, we regress SLP and SST anomaly fields (defined as deviations from their ensemble means) onto SPCs for each selected time period. Statistical significance is determined by where regression coefficients are significant at the 0.05 level ($p \leq 0.05$) based on a two-sided Student's t-test. These approaches are aiming to reveal large-scale atmospheric and oceanic linkages associated with the dominant modes of sea-ice internal variability, and how these patterns evolve over time.

**Statistical methods**

We use Pearson correlation analysis to quantify relationships between variables of interest. Correlation coefficients are considered statistically significant when the associated p-value is less than 0.05. To calculate the long-term trend, we perform a least

square analysis. The trend is considered statistically significant when its *p*-value is less 0.05 based on the two-sided Student's t-test.

## Data availability

The simulation datasets used in this study can be downloaded on public websites. CESM2-LE: https://gdex.ucar.edu/datasets/d651056/. CESM2 single forcings: https://gdex.ucar.edu/datasets/d651055/. CESM1-LE: https://www.cesm.ucar.edu/community-projects/lens/data-sets. CESM1.3-HR: https://ihesp.github.io/archive/products/ds_archive/Sunway_Runs.html. SMILEs: https://www.cesm.ucar.edu/community-projects/mmlea. DAMIP: https://esgf-node.llnl.gov/projects/cmip6. Sea-ice observation data is available from NSIDC website: https://doi.org/10.7265/a98x-0f50.

## Code availability

The Python scripts for processing data and plotting figures are available on S.-M. Tsao's Zenodo repository https://zenodo.org/records/19104702.

## Completing interests

The authors declare no competing interests.

## Corresponding author

Correspondence to Dr. Yu-Chiao Liang (pamip.yuchiao@gmail.com; yuchiaoliang@ntu.edu.tw)

## Acknowledgements

S.-M. Tsao and Y.-C. Liang are supported by grants from the National Science and Technology Council (NSTC 114-2628-M-002-001 and 114-2119-M-002-028) to National Taiwan University. We thank Drs Min-Hui Lo and Yen-Ting Hwang at National Taiwan University and Prof. Jennifer E. Kay at the University of Colorado for their constructive comments and suggestions to improve the quality of this manuscript. We would like to acknowledge high-performance computing support from the Derecho system (doi:10.5065/qx9a-pg09) provided by the NSF National Center for Atmospheric Research (NCAR), sponsored by the National Science Foundation. We thank to National Center for High performance Computing (NCHC) of National Applied Research Laboratories (NARLabs) in Taiwan for providing computational and storage resources.

## Author contributions

S.-M. Tsao, Y.-C. Liang conceived the study with encouragements and informative comments from C. Deser, and J.-Y. Yu. S.-M. Tsao performed the analyses and plotted figures. C. Deser hosted S.-M. Tsao to visit NCAR during the summer of 2024 for analysis and in-depth discussion. S.-M. Tsao and Y.-C. Liang prepared the initial manuscript draft

and all authors contributed to the manuscript writing and revising. All authors contributed equally to the interpretation of the results.

# Figures

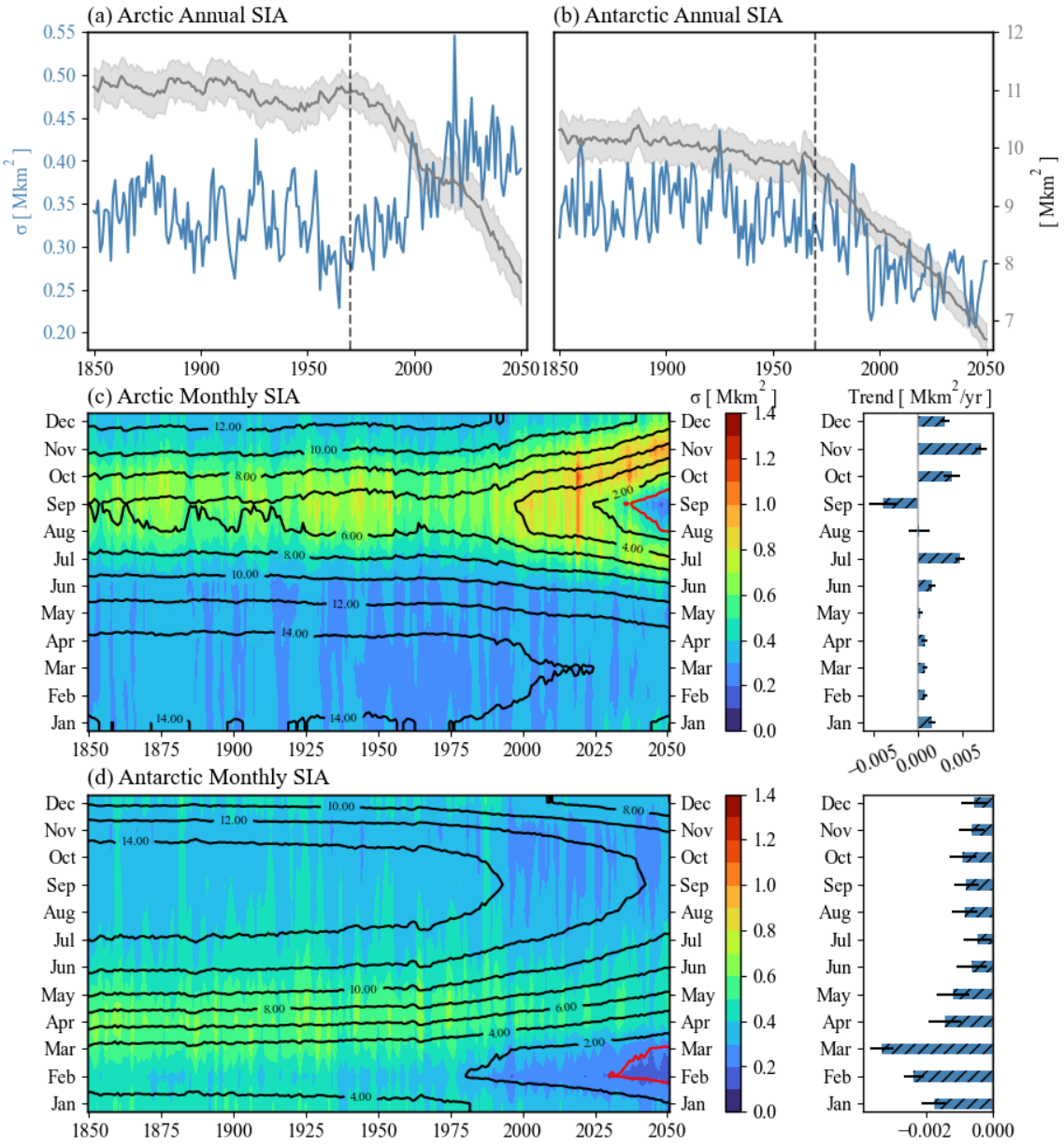


**Fig. 1: Time series and trends of Arctic and Antarctic sea-ice internal variability from 1850 to 2050 simulated in CESM2 Large Ensembles. a** Time series of annual

Arctic sea-ice area (SIA) internal variability (blue line), estimated as one standard deviation across ensemble members. The grey line indicates the ensemble-mean SIA, and the light grey shading represents the ensemble spread (±1 standard deviation). **b** Same as **a**, but for Antarctic SIA internal variability. **c** Monthly Arctic SIA internal variability (color shading), overlaid with ensemble-mean SIA values (black contours) and the ice-free condition (SIA < 1 million $km^2$) is indicated by the red contour (left panel). The right panel shows the linear trend from 1970 to 2050 for each month (bars). Hatched bars indicate statistically significant trends, and the 5–95% confidence intervals are shown by horizontal lines. **d** Same as **c**, but for Antarctic monthly SIA internal variability.

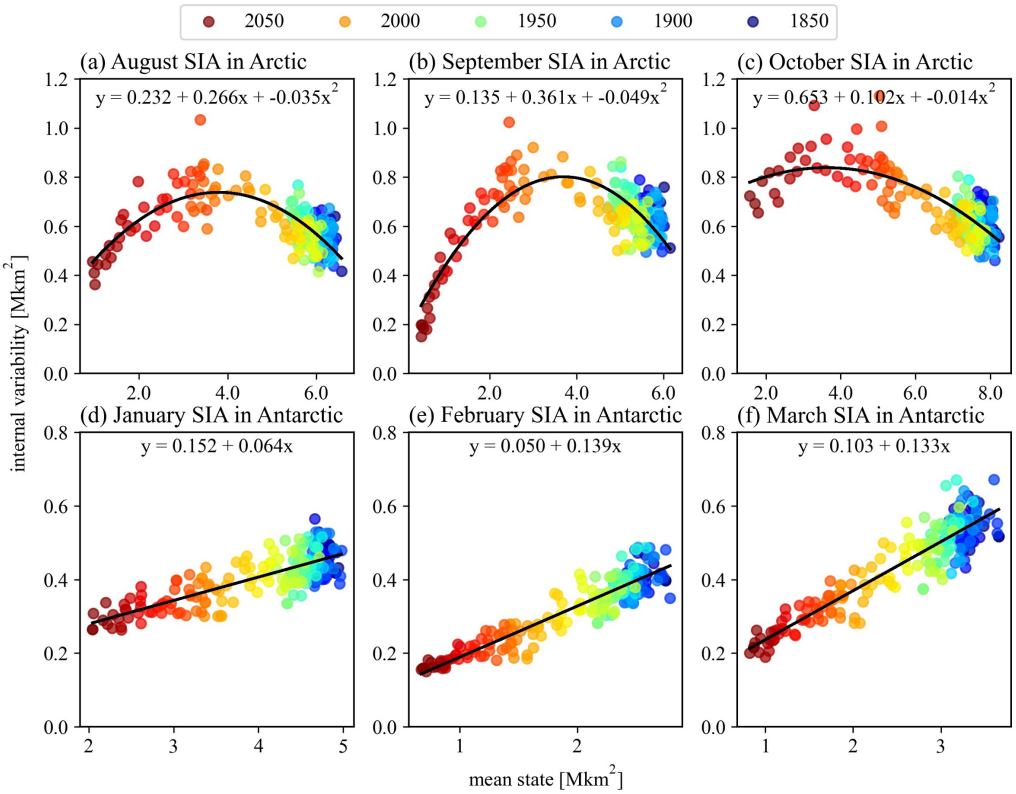


574

575 **Fig. 2: The relationships between sea-ice internal variability and ensemble-mean sea-ice**
576 **area (SIA) in summer seasons from 1850 to 2050. a** Arctic SIA in August. **b** Arctic SIA in
577 September. **c** Arctic SIA in October. **d** Antarctic SIA in January. **e** Antarctic SIA in February.
578 **f** Antarctic SIA in March. Colors indicate the corresponding decade throughout the analysis
579 period. A second-order polynomial fit is applied to the Arctic cases, whereas a linear fit is
580 applied to the Antarctic cases.

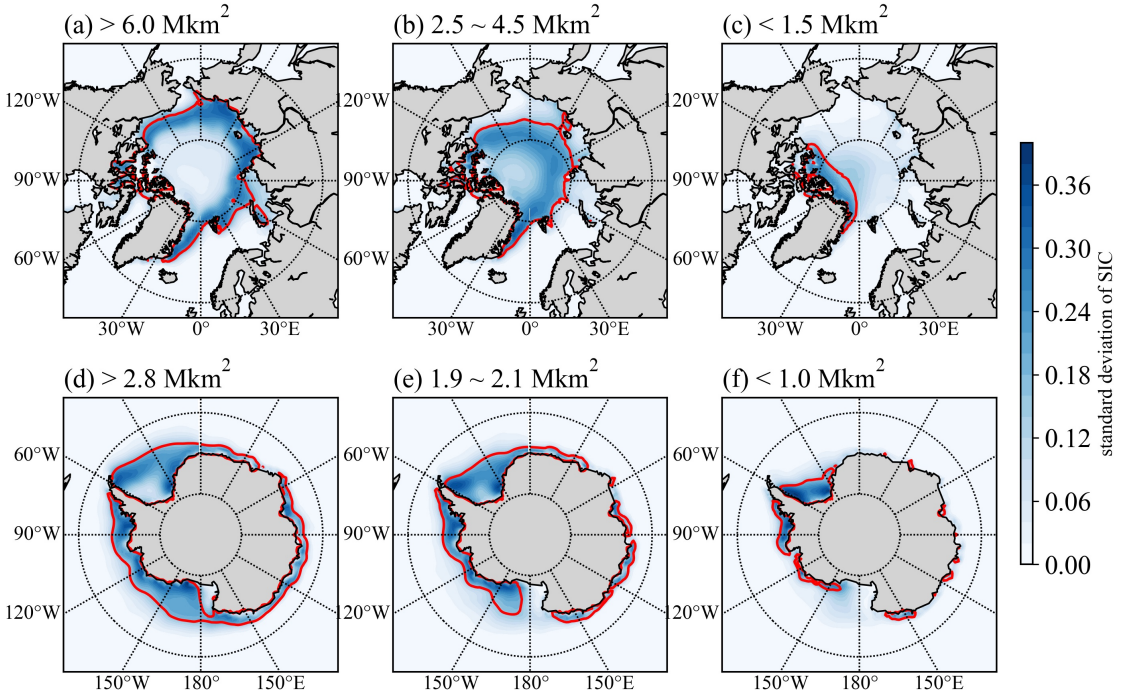


581

582 **Fig. 3: Spatial distributions of sea-ice concentration (SIC) internal variability,**
583 **categorized by different levels of ensemble-mean sea-ice area (SIA) in the Arctic**
584 **and Antarctic. a** Arctic ensemble-mean SIA > 6 million km$^2$. **b** Arctic ensemble-mean SIA
585 between 2.5 and 4.5 million km$^2$. **c** Arctic ensemble-mean SIA < 1.5 million km$^2$. **d**
586 Antarctic ensemble-mean SIA > 2.8 million km$^2$. **e** Antarctic ensemble-mean SIA between
587 1.9 and 2.1 million km$^2$. **f** Antarctic ensemble-mean SIA < 1.0 million km$^2$. The red contour
588 line in each panel indicates the sea-ice edge, defined as the ensemble-mean SIC of 15%.

589

590

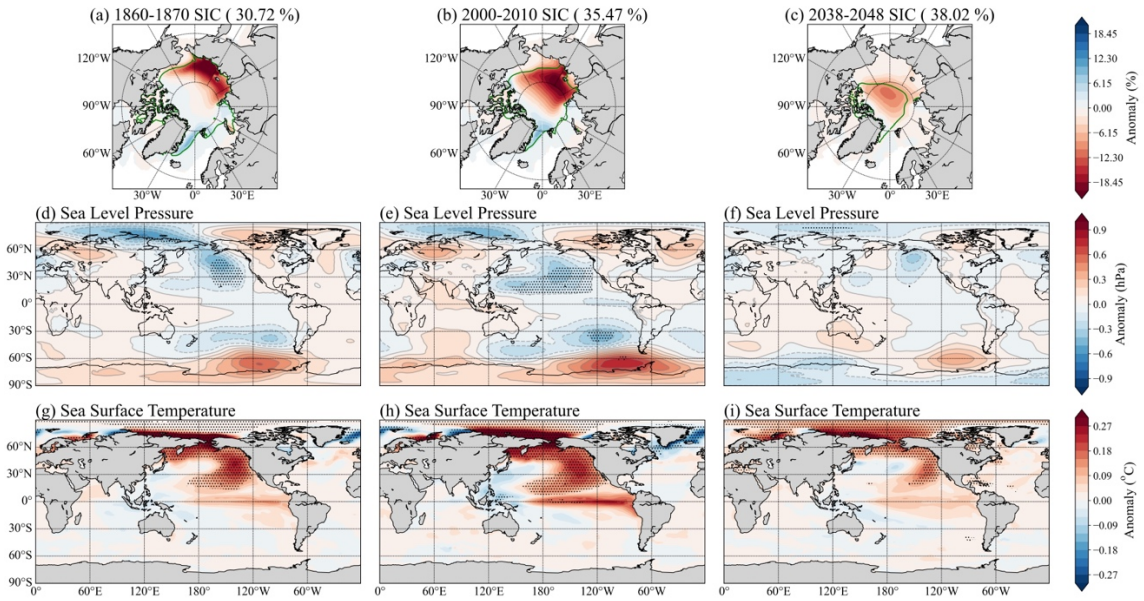


591

592 **Fig. 4: Leading mode of snapshot empirical orthogonal function (SEOF) analysis on**
593 **Arctic sea-ice concentration (SIC) averaged over August–October period, and its**
594 **associated sea-level pressure (SLP) and sea-surface temperature (SST) anomaly**
595 **patterns. a** The regressed spatial pattern of the leading SIC SEOF mode during 1860–
596 1870. The green contour indicates the sea-ice edge, defined as the ensemble-mean SIC of
597 15%. **d** The regression map of SLP onto the principal component of the leading SIC SEOF
598 mode. Stippling indicates regions where the regression coefficient is statistically
599 significant ($p$ value < 0.05) in at least 7 of the 10 years. **g** Same as **d**, but for SST. **b, e, h**
600 and **c, f, i** are the same as **a, d, g**, but for the 2000–2010 and 2038–2048 periods,
601 respectively.

602

603

604

605

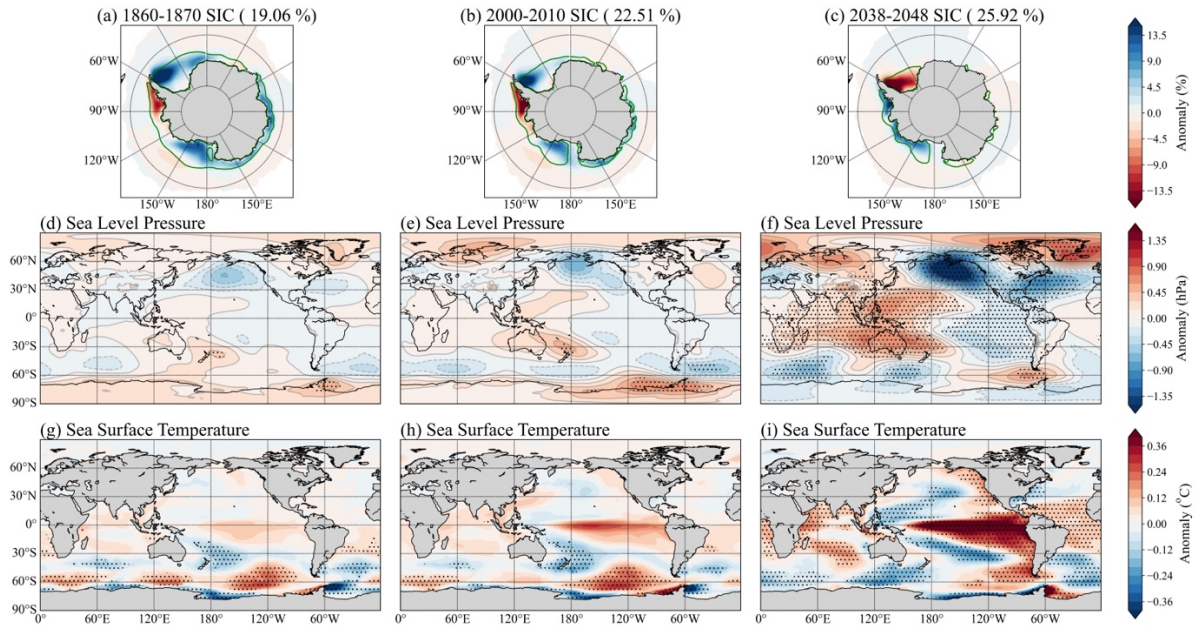


606

607 **Fig. 5: Leading mode of snapshot empirical orthogonal function (SEOF) analysis of**
608 **Antarctic sea-ice concentration (SIC) averaged over January-March, and its**
609 **associated sea level pressure (SLP) and sea-surface temperature (SST) anomaly**
610 **patterns. a** The regressed spatial pattern of the leading SIC SEOF mode during 1860–
611 1870. The green contour indicates the sea-ice edge, defined as the ensemble-mean SIC of
612 15%. **d** The regression map of SLP onto the principal component of the leading SIC SEOF
613 mode. Stippling indicates regions where the regression coefficient is statistically
614 significant ($p$ value < 0.05) in at least 7 of the 10 years. **g** Same as **d**, but for SST. **b, e, h**
615 and **c, f, i** are the same as **a, d, g**, but for the 2000–2010 and 2038–2048 periods,
616 respectively.

617

618

# References


1. Climate Change 2023: Synthesis Report. Contribution of Working Groups I, II and III to the Sixth Assessment Report of the Intergovernmental Panel on Climate Change [Core Writing Team, H. Lee and J. Romero (eds.)]. IPCC, Geneva, Switzerland, pp. 35-115 (2023).
2. Regehr, E.V., Lunn, N.J., Amstrup, S.C. & Stirling, I. Effects of earlier sea ice breakup on survival and population size of polar bears in western Hudson Bay. *J. Wildl. Manage.* **71**, 2673–2683 (2007).
3. Laidre, K.L., Stirling, I., Lowry, L.F., Wiig, Ø., Heide-Jørgensen, M.P. & Ferguson, S.H. Quantifying the sensitivity of Arctic marine mammals to climate-induced habitat change. *Ecol. Appl.* **18**, S97–S125 (2008).
4. Hollowed, A. B., Planque, B. & Loeng, H. Potential Movement of Fish and Shellfish Stocks From the Sub-Arctic to the Arctic Ocean. *Fish. Oceanogr.* **22**, 355–370 (2013).
5. Renaut, S., Devred, E. & Babin, M. Northward expansion and intensification of phytoplankton growth during the early ice-free season in Arctic. *Geophys. Res. Lett.* **45**, 10,590–10,598 (2018).
6. Ingvaldsen, R.B., Assmann, K.M., Primicerio, R. et al. Physical manifestations and ecological implications of Arctic Atlantification. *Nat. Rev. Earth Environ.* **2**, 874–889 (2021).
7. Nielsen, D.M., Pieper, P., Barkhordarian, A. et al. Increase in Arctic coastal erosion and its sensitivity to warming in the twenty-first century. *Nat. Clim. Chang.* **12**, 263–270 (2022).
8. Irrgang, A.M., Bendixen, M., Farquharson, L.M. et al. Drivers, dynamics and impacts of changing Arctic coasts. *Nat. Rev. Earth Environ.* **3**, 39–54 (2022).

9. Schiermeier, Q. The Kyoto Protocol: Hot air. *Nature* **491**, 656–658 (2012).
10. Melia, N., Haines, K. & Hawkins, E. Sea ice decline and 21st century trans-Arctic shipping routes. *Geophys. Res. Lett.* **43**, 9720–9728 (2016).
11. Doddridge E. W, Hobbs W. R et al. Impacts of Antarctic summer sea-ice extremes, *PNAS Nexus* **4**, (2025).
12. Smith, D.M. et al. Atmospheric response to Arctic and Antarctic sea ice: The importance of ocean–atmosphere coupling and the background state. *J. Climate* **30**, 4547–4565 (2017).
13. England, M.R. et al. Contrasting the Antarctic and Arctic Atmospheric Responses to Projected Sea Ice Loss in the Late Twenty-First Century. *J. Climate* **31**, 6353–6370 (2018).
14. Maksym, T. Arctic and Antarctic sea ice change: contrasts, commonalities, and causes. *Annu. Rev. Mar. Sci.* **11**, 187–213 (2019).
15. England, M.R. *et al.* Tropical climate responses to projected Arctic and Antarctic Sea-Ice loss. *Nat. Geosci.* **13**, 275–281 (2020).
16. Iles, C.E., Samset, B.H. & Lund, M.T. How polar-midlatitude atmospheric teleconnections depend on regional sea ice fraction and global warming level. *Earth Syst. Dyn.* **16**, 2253–2272 (2025).
17. Kim, H. et al. Arctic sea ice loss as a potential trigger for Central Pacific El Niño events. *Geophys. Res. Lett.* **47**, e2020GL08702 (2020).
18. Liu, J., Song, M., Zhu, Z. et al. Arctic sea-ice loss is projected to lead to more frequent strong El Niño events. *Nat. Commun.* **13**, 4952 (2022).
19. Liu, J. & Zhu, Z. Projected Antarctic sea ice change contributes to increased occurrence of strong El Niño. *npj Clim. Atmos. Sci*. **7**, 233 (2024).
20. Deng, J. & Dai, A. Arctic sea ice–air interactions weaken El Niño–Southern Oscillation.

668 *Sci. Adv.* **10**, eadk3990 (2024).
669 21. Wu, Y., Sun, L., & Terry, O. Can Arctic Sea Ice Melting Lead to More Summertime Heat
670 Extremes. *Geophys. Res. Lett.* **52**, e2025GL116668 (2025).
671 22. Barkhordarian, A., Nielsen, D.M., Olonscheck, D. et al. Arctic marine heatwaves forced
672 by greenhouse gases and triggered by abrupt sea-ice melt. *Commun. Earth Environ.* **5**,
673 57 (2024).
674 23. Duo, Y., & Zhang, J. Arctic ice loss is delaying monsoon retreat over the Indochina
675 Peninsula. *npj Clim. Atmos. Sci*. **8**, 364 (2025).
676 24. Cvijanovic, I., Simon, A., Levine, X. et al. Arctic sea-ice loss drives a strong regional
677 atmospheric response over the North Pacific and North Atlantic on decadal scales.
678 *Commun. Earth Environ.* **6**, 154 (2025).
679 25. Xu, M., Kang, S., Screen, J.A. et al. Ocean-atmosphere coupling enhances Eurasian
680 cooling in response to historical Barents-Kara sea-ice loss. *npj Clim. Atmos. Sci*. **8**, 318
681 (2025).
682 26. Pistone, K., Eisenman, I., & Ramanathan, V. Observational determination of albedo
683 decrease caused by vanishing Arctic sea ice. *Proc. Natl. Acad. Sci. U.S.A.* **111**, 3322-
684 3326 (2014).
685 27. Zhang, R. Mechanisms for low-frequency variability of summer Arctic sea ice extent,
686 *Proc. Natl. Acad. Sci. U.S.A.* **112**, 4570-4575 (2015).
687 28. Goosse, H., Kay, J.E., Armour, K.C. et al. Quantifying climate feedbacks in polar regions.
688 *Nat. Commun.* **9**, 1919 (2018).
689 29. Duspayev, A., Flanner, M. G., & Riihelä,A. Earth's sea ice radiative effect from 1980 to
690 2023. *Geophys. Res. Lett.* **51**, e2024GL109608 (2024).
691 30. Zhou, C., Wang, Q. & Tan, I. et al. Sea ice pattern effect on Earth's energy budget is
692 characterized by hemispheric asymmetry. *Sci. Adv.* **11**, eadr4248 (2025).

31. Stroeve, J. & Notz, D. Changing state of Arctic sea ice across all seasons. *Environ. Res. Lett.* **13**, 103001 (2018).
32. Yu, L., Bi, H., Zhong, S. et al. Decelerated Arctic Sea ice loss triggered by accelerated North Pacific warming over the past decade. Commun Earth Environ. 6, 922 (2025).
33. England, M. R., Polvani, L. M., Screen, J., & Chan, A. C. Minimal Arctic sea ice loss in the last 20 years, consistent with internal climate variability. *Geophys. Res. Lett.* **52**, e2025GL116175 (2025).
34. Eayrs, C., Li, X., Raphael, M.N. et al. Rapid decline in Antarctic sea ice in recent years hints at future change. *Nat. Geosci.* **14**, 460–464 (2021).
35. Fetterer, F., Knowles, K., Meier, W. N., Savoie, M., Windnagel, A. K. & Stafford, T. Sea Ice Index. (G02135, Version 4). [Data Set]. Boulder, Colorado USA. National Snow and Ice Data Center. https://doi.org/10.7265/a98x-0f50 (2025).
36. Li, X., Cai, W., Meehl, G.A. et al. Tropical teleconnection impacts on Antarctic climate changes. *Nat. Rev. Earth Environ.* **2**, 680–698 (2021).
37. Purich, A., Doddridge, E.W. Record low Antarctic sea ice coverage indicates a new sea ice state. *Commun. Earth Environ.* **4**, 314 (2023).
38. Kusahara, K. and Tatebe, H. Causes of the abrupt and sustained 2016–2023 Antarctic sea-ice decline: A sea ice–ocean model perspective. *Geophys. Res. Lett.* **52**, e2025GL115256 (2025).
39. Deser, C., Lehner, F., Rodgers, K.B. et al. Insights from Earth system model initial-condition large ensembles and future prospects. *Nat. Clim. Chang.* **10**, 277–286 (2020).
40. Mioduszewski, J. R., Vavrus, S., Wang, M., Holland, M. & Landrum, L. Past and future interannual variability in Arctic sea ice in coupled climate models. *Cryosphere* **13**, 113–124 (2019).

41. Goosse, H., Arzel, O., Bitz, C. M., de Montety, A. & Vancoppenolle, M. Increased variability of the Arctic summer ice extent in a warmer climate. *Geophys. Res. Lett.* **36**, L23702 (2009).
42. Wu, Q., Ma, Y., Hu, A. et al. Pacific sub-decadal sea surface temperature variations contributed to recent Antarctic Sea ice decline trend. *Nat. Commun.* **16**, 3386 (2025).
43. Deser, C., Phillips, A., Bourdette, V. & Teng, H. Uncertainty in climate change projections: the role of internal variability. *Clim. Dyn.* **38**, 527–546 (2012).
44. Ding, Q., Wallace, J., Battisti, D. et al. Tropical forcing of the recent rapid Arctic warming in northeastern Canada and Greenland. *Nature* **509**, 209–212 (2014).
45. Notz, D. How well must climate models agree with observations? *Phil. Trans. R. Soc. A* **373**, 20140164 (2015).
46. Bordoni, S., Kang, S.M., Shaw, T.A. et al. The futures of climate modeling. *npj Clim. Atmos. Sci.* **8**, 99 (2025).
47. Simpson, I. R. et al. Confronting Earth system model trends with observations. *Sci. Adv.* **11**, eadt8035 (2025).
48. Kay, J.E., Holland, M.M. and Jahn, A. Inter-annual to multi-decadal Arctic Sea ice extent trends in a warming world. *Geophys. Res. Lett.* **38**, L15708 (2011).
49. Swart, N., Fyfe, J., Hawkins, E. et al. Influence of internal variability on Arctic sea-ice trends. *Nat. Clim. Chang.* **5**, 86–89 (2015).
50. Holland, M. M. & Stroeve, J. Changing seasonal sea ice predictor relationships in a changing Arctic climate. *Geophys. Res. Lett.* **38**, L18501 (2011).
51. Jahn, A., Kay, J. E., Holland, M. M. & Hall, D. M. How predictable is the timing of a summer ice-free Arctic? *Geophys. Res. Lett.* **43**, 9113–9120 (2016).

52. Shen, Z., A. Duan, W. Zhou, Y. Peng, and J. Li. Reconciling Roles of External Forcing and Internal Variability in Arctic Sea Ice Change on Different Time Scales. *J. Climate* **37**, 3577–3591 (2024).
53. Siew, P.Y.F., Wu, Y., Ting, M. et al. Significant contribution of internal variability to recent Barents–Kara sea ice loss in winter. *Commun. Earth Environ.* **5**, 411 (2024).
54. Deser, C. Certain uncertainty: the role of internal climate variability in projections of regional climate change and risk management. *Earth's Future* **8**, e2020EF001854 (2020).
55. Zhang, X., Vihma, T., Rinke, A. et al. Weather and climate extremes in a changing Arctic. *Nat. Rev. Earth Environ.* 6, 691–711 (2025).
56. Rodgers, K. B. et al. Ubiquity of human-induced changes in climate variability. *Earth Syst. Dynam.* **12**, 1393–1411 (2021).
57. Hawkins, E., Smith, R. S., Gregory, J. M. and Stainforth, D. A. Irreducible uncertainty in near-term climate projections. *Clim. Dyn.* **46**, 3807–3819 (2016).
58. Machete, R. L. & Smith, L. A. Demonstrating the value of larger ensembles in forecasting physical systems. *Tellus A* **68**, 28393 (2016).
59. Bengtsson, L. & Hodges, K. I. Can an ensemble climate simulation be used to separate climate change signals from internal unforced variability? *Clim. Dyn.* **52**, 3553–3573 (2019).
60. Eisenman, I. Geographic muting of changes in the Arctic sea ice cover. *Geophys. Res. Lett.* **37**, L16501 (2010).
61. Danabasoglu, G. et al. The Community Earth System Model version 2 (CESM2). *J. Adv. Modeling Earth Syst.* **12**, e2019MS001916 (2020).

62. Kay, J. E. et al. Less surface sea ice melt in the CESM2 improves Arctic sea ice simulation with minimal non-polar climate impacts. *J. Adv. Model. Earth Syst.* **14**, e2021MS002679 (2022).
63. Chang, P. et al. An unprecedented set of high-resolution earth system simulations for understanding multiscale interactions in climate variability and change. *J. Adv. Model. Earth Syst.* **12**, e2020MS002298 (2020).
64. Bitz, C. M. & Roe, G. H. A mechanism for the high rate of sea ice thinning in the Arctic Ocean. *J. Climate* **17**, 3623–3632 (2004).
65. Massonnet, F., Vancoppenolle, M., Goosse, H. et al. Arctic sea-ice change tied to its mean state through thermodynamic processes. *Nat. Clim. Chang.* **8**, 599–603 (2018).
66. Liang, Y.-C. et al. Impacts of Arctic sea ice on cold season atmospheric variability and trends estimated from observations and a multimodel large ensemble. *J. Climate* **34**, 8419–8443 (2021).
67. Zhu, T. & Yu, J.Y. A Shifting Tripolar Pattern of Antarctic Sea Ice Concentration Anomalies During Multi-Year La Niña Events. *Geophys. Res. Lett.* **49**, e2022GL101217 (2022).
68. Dörr, J.S., Bonan, D.B., Årthun, M., Svendsen, L., & Wills, R.C.J. Forced and internal components of observed Arctic sea-ice changes. *The Cryosphere* **17**, 4133–4153 (2023).
69. Bonan, D. B. et al. Sources of low-frequency variability in observed Antarctic sea ice. *The Cryosphere* **18**, 2141–2159 (2024).
70. Morioka, Y., Zhang, L., Cooke, W. et al. Role of anthropogenic forcing in Antarctic sea ice variability simulated in climate models. *Nat. Commun.* 15, 10511 (2024).

71. Zhu, T., Yu, J. Saltzman, E. S., and Tseng, L. Distinct Impacts of Multiyear El Niño on Antarctic Sea Ice Concentration due to Atlantic and Indian Ocean Conditions. *J. Climate* **38**, 2063–2077 (2025).
72. Wang, C., Su, H., Zhai, C. et al. Recent slowing of Arctic sea ice melt tied to multidecadal NAO variability. *Nat. Commun.* **16**, 8504 (2025).
73. Siew, P.Y. et al. Identifying physical drivers of Arctic sea ice growth and their changing roles in a warming climate. *Geophys. Res. Lett.* **52**, (2025).
74. O'Brien, J. P. & Deser. C. Quantifying and Understanding Forced Changes to Unforced Modes of Atmospheric Circulation Variability over the North Pacific in a Coupled Model Large Ensemble. *J. Climate* **36**, 19–37 (2023).
75. Deser, C., Alexander, M. A., Xie S.-P., & Phillips, A. S. Sea surface temperature variability: Patterns and mechanisms. *Annu. Rev. Mar. Sci.* **2**, 115–143 (2010).
76. Peings, Y. and Magnusdottir, G. Forcing of the wintertime atmospheric circulation by the multidecadal fluctuations of the North Atlantic ocean. *Environ. Res. Lett.* **9**, 034018 (2014).
77. Rogers, J. C. The North Pacific Oscillation. *Int. J. Climatol.* **1**, 39–57 (1981).
78. Di Lorenzo, E., Schneider, N., Cobb, K. M., Franks, P. J. S., Chhak, K., Miller, A. J., McWilliams, J. C., Bograd, S. J., Arango, H., Curchitser, E., Powell, T. M., & Rivière, P.: North Pacific Gyre Oscillation links ocean climate and ecosystem change. *Geophys. Res. Lett.* **35**, L08607 (2008).
79. Kug, J., F. Jin, and S. An. Two Types of El Niño Events: Cold Tongue El Niño and Warm Pool El Niño. *J. Climate* **22**, 1499–1515 (2010).
80. Bonan, D. B. & Blanchard-Wrigglesworth, E. Nonstationary teleconnection between the Pacific Ocean and Arctic sea ice. *Geophys. Res. Lett.* **47**, e2019GL085666 (2020).

81. Chen, J. et al. ENSO's changing grip on Bering Sea ice: The emerging control of the North Pacific meridional mode. *Sci. Adv.* **11**, eady2329 (2025).
82. Stroeve, J. & Notz, D. Changing state of Arctic sea ice across all seasons. Environ. Res. Lett. **13**, 103001 (2018).
83. Jahn, A., Holland, M.M. & Kay, J.E. Projections of an ice-free Arctic Ocean. *Nat. Rev. Earth Environ.* **5**, 164–176 (2024).
84. Eisenman, I., Schneider, T., Battisti, D. S. & Bitz, C. M., Consistent changes in the sea ice seasonal cycle in response to global warming. *J. Climate* **24**, 5325–5335 (2011).
85. Horvat, C. Marginal ice zone fraction benchmarks sea ice and climate model skill. *Nat. Commun.* **12**, 2221 (2021).
86. Roach, L.A. and Polvani, L.M. Persistent antarctic sea ice biases in CMIP6 models in spite of the recent decade-long sharp decline. *J. Climate* **39**, 1669–1679 (2026).
87. Bitz, C. M., M. M. Holland, E. C. Hunke, and R. E. Moritz, Maintenance of the Sea-Ice Edge. *J. Climate* **18**, 2903–2921 (2005).
88. Aylmer, J., Ferreira, D. & Feltham, D. Impacts of oceanic and atmospheric heat transports on sea ice extent. *J. Climate* **33**, 7197-7215 (2020).
89. Aylmer, J.R., Ferreira, D. & Feltham, D.L. Impact of ocean heat transport on sea ice captured by a simple energy balance model. *Commun. Earth Environ.* **5**, 406 (2024).
90. Di Lorenzo, E., Cobb, K., Furtado, J. et al. Central Pacific El Niño and decadal climate change in the North Pacific Ocean. *Nat. Geosci.* **3**, 762–765 (2010).
91. Wettstein, J. J. & Deser, C. Internal variability in projections of twenty-first century Arctic sea ice loss: role of the large-scale atmospheric circulation. *J. Climate* **27**, 527–550 (2014).
92. Wang, S. et al. Contribution of the deepened Amundsen Sea low to the record low Antarctic sea ice extent in February 2022. *Environ. Res. Lett.* **18**, 054002 (2023).

93. Chang, P., Fang, Y., Saravanan, R. et al. The cause of the fragile relationship between the Pacific El Niño and the Atlantic Niño. *Nature* **443**, 324–328 (2006).
94. Li, X., Xie, SP., Gille, S. et al. Atlantic-induced pan-tropical climate change over the past three decades. *Nat. Clim. Chang.* **6**, 275–279 (2016).
95. Hong, J., S. Yeh, and Y. Yang. Interbasin Interactions between the Pacific and Atlantic Oceans Depending on the Phase of Pacific Decadal Oscillation and Atlantic Multidecadal Oscillation. *J. Climate* **35**, 2883–2894 (2022).
96. Richter, I. et al. The Tropical Basin Interaction Model intercomparison project (TBIMIP). *Geosci. Model Dev.* **18**, 2587–2608 (2025).
97. Miao, Y. et al. Impact of inter-basin interactions on enso-associated hadley circulation adjustments. *Geophys. Res. Lett.* **53**, (2026).
98. Simpson, I. R. et al. The CESM2 Single-Forcing Large Ensemble and Comparison to CESM1: Implications for Experimental Design. *J. Climate* **36**, 5687–5711 (2023).
99. DeRepentigny, P. et al. Enhanced simulated early 21st century Arctic sea ice loss due to CMIP6 biomass burning emissions. *Sci. Adv.* **8,** (2022).
100. Kay, J.E. et al. The Community Earth System Model (CESM) Large Ensemble Project: A Community Resource for studying climate change in the presence of internal climate variability. *Bull. Am. Meteorol. Soc.* **96**, 1333–1349 (2015).
101. Xu, G., Rencurrel, M.C., Chang, P. et al. High-resolution modelling identifies the Bering Strait's role in amplified Arctic warming. *Nat. Clim. Chang.* **14**, 615–622 (2024).
102. Fol, M., Tremblay, B., Pfirman, S. et al. Revisiting the Last Ice Area projections from a high-resolution Global Earth System Model. *Commun. Earth Environ.* **6**, 46 (2025).
103. Jeffrey, S., Rotstayn, L., Collier, M., Dravitzki, S., Hamalainen, C., Moeseneder, C., et al. Australia's CMIP5 submission using the CSIRO-Mk3.6 model. *Australian Meteorological and Oceanographic* **63**, 1–14 (2013).

104. Sun, L., Alexander, M., & Deser, C. Evolution of the global coupled climate response to Arctic sea ice loss during 1990–2090 and its contribution to climate change. *J. Climate* **31**, 7823–7843 (2018).

105. Rodgers, K. B., Lin, J., & Frölicher, T. L. Emergence of multiple ocean ecosystem drivers in a large ensemble suite with an Earth System Model. *Biogeosciences* **12**, 3301–3320 (2015).

106. Maher, N., Milinski, S., Suarez-Gutierrez, L., Botzet, M., Dobrynin, M., Kornblueh, L., et al. The max Planck Institute grand ensemble: Enabling the exploration of climate system variability. *J. Adv. Model. Earth Syst.* **11**, 2050–2069 (2019).

107. Wu, Y. et al. Exploiting smiles and the CMIP5 archive to understand Arctic climate change seasonality and uncertainty. *Geophys. Res. Lett.* **50**, e2022GL100745 (2023).

108. Wyburn-Powell, C., Jahn, A. & England, M. R.. Modeled Interannual Variability of Arctic Sea Ice Cover is within Observational Uncertainty. *J. Climate* **35**, 6827–6842 (2022).

109. Gillett, N. P. et al. The detection and attribution model intercomparison project (DAMIP v1. 0) contribution to CMIP6. *Geosci. Model. Dev.* **9**, 3685–3697 (2016).

110. Eyring, V. et al. Overview of the coupled model Intercomparison project phase 6 (CMIP6) experimental design and organization. *Geosci. Model. Dev.* **9**, 1937–1958 (2016).

111. Shiogama, H. et al. MIROC6 Large Ensemble (MIROC6-LE): experimental design and initial analyses. *Earth Syst. Dynam.* **14**, 1107–1124 (2023).

112. Swart, N. C. et al. The Canadian Earth System Model version 5 (CanESM5.0.3), *Geosci. Model Dev.* **12**, 4823–4873 (2019).

113. Wu, Y.T., Liang, Y.C., Previdi, M. et al. Stronger Arctic amplification from anthropogenic aerosols than from greenhouse gases. *npj Clim. Atmos. Sci.* **7**, 142 (2024).

114. Liu, Z.F. et al. Anthropogenic intensification of Arctic anticyclonic circulation. *Sci. Adv.* **11**, eads4508 (2025).

115. Haszpra, T., Herein, M. & Bódai, T. Investigating ENSO and its teleconnections under climate change in an ensemble view-A new perspective. *Earth Syst. Dyn.* **11**, 267–280 (2020).

116. North, G. R., Bell, T. L., Cahalan, R. F. & Moeng F. J. Sampling errors in the estimation of empirical orthogonal functions. *Mon. Wea. Rev.* **110**, 699–706 (1982).